RESEARCH ARTICLE

Key Points:
- Spectral aerosol optical thickness retrieval algorithm was developed based on the Langley calibration method
- Developed empirical stray light correction method considerably improved aerosol optical thickness retrievals at ultraviolet wavelengths
- Retrieved spectral aerosol optical thickness provides the key constraints for additional aerosol properties and trace gas retrievals

Correspondence to:
U. Jeong,
ukkyo.jeong@nasa.gov

Langley Calibration Analysis of Solar Spectroradiometric Measurements: Spectral Aerosol Optical Thickness Retrievals

Ukkyo Jeong[1,2] , Si-Chee Tsay[2], Peter Pantina[2,3], James J. Butler[2], Adrian M. Loftus[1,2] , Nader Abuhassan[2,4], Jay R. Herman[2,4] , Alexander Dimov[2,3], Brent N. Holben[2], and Robert J. Swap[2]

[1]Earth System Science Interdisciplinary Center, University of Maryland, College Park, MD, USA, [2]NASA Goddard Space Flight Center, Greenbelt, MD, USA, [3]Science Systems and Applications Inc., Lanham, MD, USA, [4]Joint Center for Earth Systems Technology, University of Maryland Baltimore County, Baltimore, MD, USA

Abstract Aerosol optical thickness (τ_{aer}) is a fundamental parameter for analyzing aerosol loading and associated radiative effects. The τ_{aer} can constrain many inversion algorithms using passive/active sensor measurements to retrieve other aerosol properties and/or the abundance of trace gases. In the next wave of spectroradiometric observations from geostationary platforms, we envision that a strategically distributed network of robust, well-calibrated ground-based spectroradiometers will comprehensively complement spaceborne measurements in spectral and temporal domains. Spectral τ_{aer} can be accurately obtained from direct-Sun measurements based on the Langley calibration method, which allows for the analysis of distinct spectral features of the calibration results. In this study, we present a spectral τ_{aer} retrieval algorithm for an in-house developed, field deployable spectroradiometer instrument covering wavelengths from ultraviolet to near-infrared (UV-Vis-NIR). The spectral total optical thickness obtained from the Langley calibration method is partitioned into molecular and particulate components by utilizing a least squares method. The resulting high temporal-resolution τ_{aer} and Ångström Exponent can be used effectively for cloud screening. The new algorithm was applied to month-long measurements acquired from the rooftop at National Aeronautics and Space Administration Goddard Space Flight Center's Building 33. The retrieved τ_{aer} demonstrated excellent agreement with those from well-calibrated Aerosol Robotic Network Sun photometers at all overlapping wavelengths (correlation coefficients higher than 0.98). In addition, empirical stray light corrections considerably improved τ_{aer} retrievals at short wavelengths in the UV. The continuous spectrum of τ_{aer} from UV-Vis-NIR spectroradiometers is expected to provide more informative constraints for retrieval of additional aerosol properties such as refractive indices, size, and bulk vertical distribution.

1. Introduction

Monitoring spatial and temporal distributions of atmospheric trace gases and aerosols is key to understanding their impacts on climate change (Intergovernmental Panel on Climate Change, 2013, and references therein) and human health (Kampa & Castanas, 2008, and references therein). Remote sensing and retrievals using hyperspectral measurements from ground-based networks and low-Earth-orbit platforms have provided extensive spatial (both vertically and horizontally) information on trace gases and aerosols (e.g., Hönninger et al., 2004; Wagner et al., 2008, and references therein). Previous and ongoing low-Earth-orbit satellite missions including the Global Ozone Monitoring Experiment (GOME) 1 and 2 (Burrows et al., 1999; Munro et al., 2016), the Scanning Imaging Absorption spectroMeter for Atmospheric CHartographY (SCIAMACHY; Bovensmann et al., 1999), and the Ozone Monitoring Instrument (OMI; Levelt et al., 2006) have successfully monitored the global distribution of atmospheric trace gases, aerosols, and clouds using these techniques. Future hyperspectral sensors under development for geostationary satellites will provide higher spatial and temporal resolution of measurements, thereby improving trace gas and aerosol retrievals across North America, Europe, and Southeast-East Asia (e.g., Ingmann et al., 2012; Tsay et al., 2016; Zoogman et al., 2017). Thus, reliable networked ground-based measurements are essential to provide independent measurements and ancillary information for calibrating and validating (or consistency checking) satellite-based products. The National Aeronautics and Space Administration (NASA) has operated intensive global ground-based networks including the Aerosol Robotic Network (AERONET) and the Micro-Pulse Lidar Network (MPLNET) largely for such purposes (e.g., Holben et al., 1998; Welton et al., 2001).

Complimenting these instruments with ground-based spectroradiometers will further enhance the monitoring capabilities and increase measurement fidelity of atmospheric trace gases and aerosols from satellites.

Spectral optical thickness of aerosol (τ_{aer}) is the basic quantity of aerosol retrieval algorithms that is related to the amount and microphysical properties of aerosol particles (e.g., Grassl, 1971; King et al., 1978; Torres et al., 2016; Yamamoto & Tanaka, 1969). Additionally, direct-Sun τ_{aer} measurements also have been used as central constraints for inversion algorithms of additional aerosol properties (e.g., size distribution, complex refractive indices, and bulk vertical distribution) that use diffuse-sky radiance or polarization measurements from the ground-based instruments (e.g., Dubovik & King, 2000; Xu et al., 2015). Such detailed information on aerosol properties helps to identify their sources and understand their radiative effects in the atmosphere (Dobovik et al., 2002). Furthermore, incorrect optical properties of aerosols are a major source of error for several trace gas retrievals, since they affect the light path length of trace gas absorption (e.g., Chimot et al., 2016; Hong et al., 2017; Torres & Bhartia, 1999). Particularly, the τ_{aer}, vertical distribution and microphysical properties of aerosols were found to be a significant factor of light path length (e.g., Hong et al., 2017; Leitão et al., 2010; Lin et al., 2014; Yang et al., 2014).

Major error sources of ground-based direct-Sun τ_{aer} retrievals include instrument stability, radiometric calibration (i.e., gain, linearity, and offset), and cloud masking methods (Holben et al., 1998; Smirnov et al., 2000). The calibration constant (or gain) of direct-Sun measurements traditionally stems from the Langley method based on the Beer-Lambert-Bouguer (B-B-L) law, which provides the top of the atmosphere (TOA) irradiance estimates for zero optical depth, as a result of a regression between air mass and surface solar irradiance (Langley, 1881). Although the Langley method is quite simple and straightforward, there are various implementation options for measured data (e.g., plotting method, other instrument calibration methods, selection of Langley events, calculation of relative air mass, gas absorptions, and Rayleigh scattering) (e.g., Holben et al., 1998; Schotland & Lea, 1986; Shaw, 1982, 1983; Slusser et al., 2000; Thomason et al., 1983; Wilson & Forgan, 1995). Therefore, development of an objective Langley calibration method will help to successfully make use of spectral information obtained from spectroradiometer measurements.

Charge-coupled device (CCD)-based instruments provide radiance measurements with high spectral resolution and sensitivity, making them useful for both trace gas and aerosol retrievals. However, since CCDs are sensitive to field conditions, such as temperature and humidity, it is important to consistently monitor and calibrate the instruments to reduce drift in errors over time. This study aims to develop a stable and effective field absolute calibration method for spectroradiometers using direct-Sun measurements. Whereas prior studies typically have implemented the Langley calibration for a single wavelength or discrete channels independently (e.g., Holben et al., 1998; Schotland & Lea, 1986; Slusser et al., 2000; Wilson & Forgan, 1995), this study uses the spectral features of Langley calibration results to take advantage of simultaneous hyperspectral measurements.

2. Instrumentation

Radiance and irradiance are the two fundamental quantities in remote sensing applications. In conjunction with the broadband radiometer array (for irradiance; Ji et al., 2011; Ji & Tsay, 2010), multiple copies of an in-house built ultraviolet-visible-near-infrared (UV-Vis-NIR) spectroradiometer (for radiance) constitute SMART (Spectral Measurements for Atmospheric Radiative Transfer, cf. https://smartlabs.gsfc.nasa.gov/) network units that facilitate a surface strategic distribution for remote sensing of atmospheric radiation (e.g., Tsay et al., 2016). The UV-Vis-NIR spectroradiometer, originally developed by the Pandora network group at NASA Goddard Space Flight Center, covers a 280- to 820-nm spectral range (with about 1-nm resolution and ~3.7x oversampling) and utilizes a small commercially available spectrometer (AvaSpec-ULS2048x64, Avantes, cf. https://www.avantes.com/) with high stability, high sensitivity, and low noise. The spectrometer uses a symmetric Czerny-Turner system with a 2,048 × 64 backthinned Hamamatsu CCD (Herman et al., 2015). The spectral range covers several gas absorption bands including O_2, O_3, NO_2, SO_2, HCHO, and H_2O (Figure 1a). Most of the major components (e.g., fore optics, Sun-and-sky tracker, and data acquisition) of the UV-Vis-NIR spectroradiometer are similar or identical to the standard Pandora spectrometer system, which is used to retrieve total columns of ozone and other trace gases in the atmosphere from direct-Sun measurements (Herman et al., 2009, 2015; Tzortziou et al., 2012).
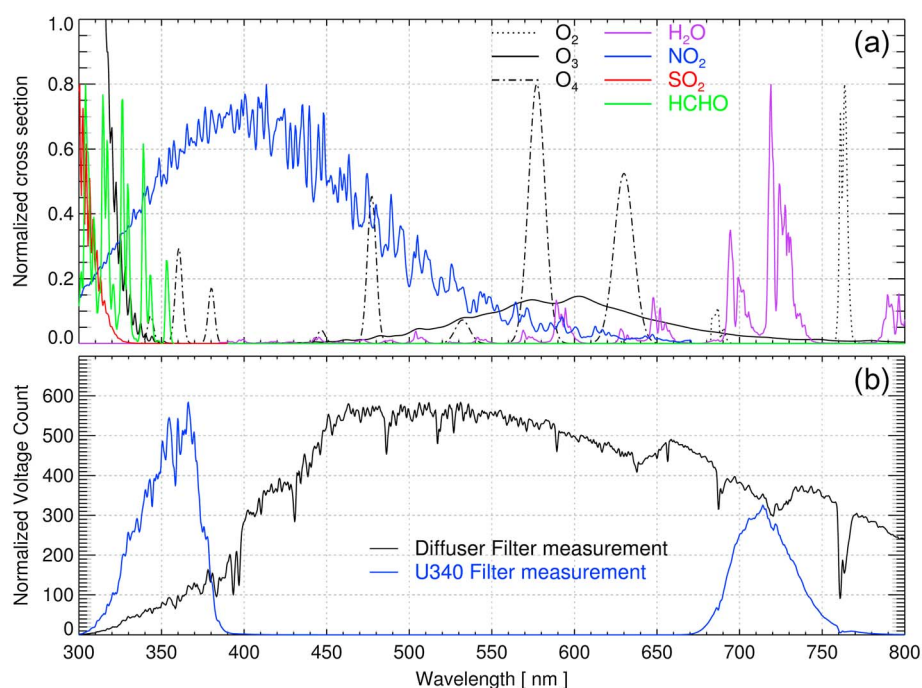
Figure 1. (a) Absorption cross sections of several atmospheric gases convolved with spectral response functions within the spectral range of UV-Vis-NIR spectroradiometer. (b) Mean voltage counts using a diffuser and U340 filter measured at the Mauna Loa Observatory (19.54°N, 155.58°W, 3,397 m altitude) on 19 May 2017. Note that plots in panels (a) and (b) were scaled to similar value for qualitative comparison.

The optical head contains two rotating filter wheels. One contains four neutral density (ND) filters (to increase dynamic range by a factor of 10^4), and the other includes a U340 filter (to block stray light from the visible spectrum), a ground-fused silica diffuser (diffuser hereafter, for trace gas and aerosol retrievals), and an opaque filter (dark current measurements) for spectral band-pass filtering. Combinations of a variable exposure time (4–4,000 ms) and ND filters yield a dynamic range up to 10^7, which allows for the radiance measurement of both direct Sun and diffuse sky throughout the day. Without clouds in direct-Sun mode, the spectroradiometer averages about 4,000 measurements in 20 s. The field of view (FOV) for direct-Sun observations using a diffuser is about 2.2°. The diffuser broadens the FOV and helps to evenly distribute light and eliminate bright spots. For sky observations without a diffuser, the FOV is about 1.6°. A 400-µm-diameter core fiber optic cable connects the optical head, which is mounted on a Sun-tracker (or sky-scanner), to the spectrometer. The spectrometer is mounted inside an insulated enclosure with thermoelectric cooling, which reduces measurement errors due to variations in spectrometer temperature (the temperature was stabilized between 19.0 and 24.5 °C during daytime in this study). An example of measured spectral mean count rate using the diffuser and U340 filter is shown in Figure 1b, which is acquired at Mauna Loa Observatory (19.54°N latitude, 155.58°W longitude, 3,397 m altitude) on 19 May 2017. Although most of the visible light is screened by U340 filter, there is a leak in the filter around 720 nm, which can cause spectral out-of-band (OOB) stray light errors in the UV measurements.

In this study, we use data measured on the rooftop of the NASA Goddard Space Flight Center Building 33 (38.99°N latitude, 76.84°W longitude) for three months from 20 October 2016 to 19 January 2017. We additionally use AERONET products (version 3.0 and level 2.0) to compare τ_{aer} retrievals from UV-Vis-NIR spectroradiometer during the measurement period. AERONET is a NASA-funded global network of automatic Sun-tracking and sky-scanning spectroradiometers (Holben et al., 1998). The instrument measures direct Sun with a 1.2° FOV at discrete channels from UV to NIR (i.e., 340, 380, 440, 500, 675, 870, 940, 1,020, and 1,640 nm). The direct-Sun measurements take about 10 s to scan all filter wheels in front of the detector for each wavelength. The filters are ion-assisted deposition interference filters with full width at half maximum of 2 nm for 340 nm, 4 nm for 380 nm, and 10 nm for all other channels. The nominal uncertainty of

τ_{aer} from AERONET is estimated to be about 0.01 in the Vis-NIR and about 0.02 in the UV channels (Eck et al., 1999). Further information on AERONET including calibration, retrieval, and cloud-screening algorithm are described in Holben et al. (1998), Smirnov et al. (2000), and Eck et al. (1999).

3. Laboratory and Field Calibrations

Accurate and consistent calibration is critical for operations of widely distributed network instruments. The NASA Pandora network group established a sophisticated, automatic calibration procedure that utilizes a variety of narrow-line and broadband emission lamps with temperature control (e.g., Herman et al., 2015). In this section, we describe additional calibration efforts that are significant for aerosol retrievals.

3.1. Linearity and Offset

Reliable radiometric calibrations of linearity, offset, and gain provide a means to produce quality τ_{aer} measurements. For example, spectroradiometer nonlinearity effects produce around 3% radiometric uncertainty at high counts; however, these effects are negligible at low counts (Herman et al., 2015). We characterized linearity in the laboratory using a stabilized 1,000 W FEL-lamp with various exposure times to find the saturation level where nonlinearity effects were significant. During operation, the exposure time was limited so as not to exceed this predetermined saturation level (Herman et al., 2015). The dark current and offset (caused by thermally excited electrons in the sensor that are incident within the conduction band that collect in the CCD wells) were corrected by subtracting the equivalent opaque filter measurement from the observations.

3.2. Filter Transmittance

To characterize the spectral transmittances of the ND filters, we measured instrument counts in the laboratory using a stabilized FEL-lamp and different combinations of ND filters. Although the filter transmittances can change over time, especially when the instrument is deployed in the field for a long period, such variations are mostly compensated by the periodic Langley calibration. The ratios of transmittances between different ND filters (hereafter, relative filter transmittance) require higher accuracy than their absolute transmittances to obtain the same gains with different ND filters. On a cloud-free morning, the position of ND filter gradually moves to more opaque filter as the air mass becomes smaller (solar intensity becomes larger). In the field, the relative filter transmittances were calculated from the ratio between two consecutive counts with different ND filter positions. Counts of prior filter positions were weighted by temporal extrapolation to later filter positions. Relative ND filter transmittances were only updated during Langley events (clear days). The recorded counts from different ND filter positions were normalized to the most frequent ND filter position during the Langley events using the obtained relative transmittances (ND3 filter in this study).

3.3. Spectral Registration

The wavelength of each detector was first registered in the laboratory using known narrow emission lines from multiple lamps that cover most of spectral range at several spectrometer temperatures (i.e., 12, 20, and 28 °C). For better stability of the wavelength registration for the entire spectral range used for aerosol retrieval (330–800 nm in this study), we performed a nonlinear least squares method to fit the instrument spectrum to a known reference spectrum after the methods of Casper and Chance (1997) and Marquardt (1963). The reference spectrum for the spectral registration is the theoretical values of spectral solar irradiance at the bottom of the atmosphere, which is calculated based on the B-B-L law using the TOA solar spectrum and atmospheric attenuation as follows:

$$F_B(\lambda) = F_T(\lambda) \exp\left(-\sum_i m_i(\lambda)\tau_i(\lambda)\right) \tag{1}$$

where $F_B(\lambda)$ and $F_T(\lambda)$ are the bottom of the atmosphere and TOA solar irradiance at wavelength λ and $m_i(\lambda)$ and $\tau_i(\lambda)$ are the relative air mass and optical thickness of the ith attenuating species in the atmosphere at λ, respectively. The relative air mass is a ratio of optical thicknesses between a known slant path to the vertical path. Rayleigh scattering and gas absorptions are factored into the calculation of the reference spectrum in equation (1). We used the recent version of Smithsonian Astrophysical Observatory reference spectrum for the $F_T(\lambda)$ (Chance & Kurucz, 2010). The sources of the gaseous cross sections are listed in Table 1.

Table 1

Absorption Cross-Section Database Sources Used for Wavelength Registration and Spectral Fitting for τ_{aer}

Species	Wavelength registration	Spectral fitting for τ_{aer}
O_2	HITRAN[a] (Rothman et al., 2013)	Langley optical thickness
O_3	Brion et al. (1993, 1998)	Brion et al. (1993, 1998)
O_4	Greenblatt et al. (1990)	Greenblatt et al. (1990)
SO_2	Vandaele et al. (1994)	Vandaele et al. (1994)
HCHO	HITRAN (Chance & Orphal, 2011)	HITRAN (Chance & Orphal, 2011)
H_2O	HITRAN (Rothman et al., 2013)	Langley optical thickness
NO_2	HITRAN (Rothman et al., 2013)	HITRAN (Rothman et al., 2013)

[a]HIgh-resolution TRANsmission molecular absorption database.

The nonlinear least squares method for the spectral registration minimizes the following cost function to force measured spectral features to converge with a known or theoretical solar spectrum and/or gas absorption bands (Casper & Chance, 1997):

$$\chi^2 = \sum_i \left[C_i - \left\{ P_0 + P_1 i + P_2 i^2 + P_3 i^3 + (1+s)f(F_B, \Phi, \lambda_i) \right\} \right]^2 \qquad (2)$$

where χ is the cost function, C_i is the measured voltage counts at ith detector, Ps are the regression coefficients of polynomials, s is the scale factor, and f is a function that returns F_B convolved with a slit function (Φ) at the wavelength modulated by shift and squeeze parameters (λ_i) as in the following equation:

$$\lambda_i = \lambda_m + d\lambda + (\lambda_f - \lambda_m)(1 + \Delta\lambda), \qquad (3)$$

where λ_f is the wavelength information before modulation, λ_m is the mean value of λ_f at a target wavelength range, and $d\lambda$ and $\Delta\lambda$ are the spectral shift and squeeze parameter, respectively. The spectral registration was performed for narrower windows (~100 nm), rather than for the whole wavelength range at a time, to improve numerical stability and to compensate for the higher-order squeeze term. An example of the spectral registration results for the three wavelength windows of the spectrometer is shown in Figure 2, where small shifts can be seen from the uncalibrated spectrum (blue) to the calibrated spectrum (red). Note that offsets between the theoretical solar spectrum and measurements are not relevant, since the measurements are acquired before radiometric calibration. The offsets are compensated by the low-order-polynomials in equation (2), and typically have negligible effects on spectral registration.

3.4. Out-Of-Field (OOF) Stray Light Correction

For typical direct-Sun measurements using a narrow FOV collimator, spatial out-of-field (OOF) stray light due to diffuse light (scattered light coming into the collimator from outside the direct beam) can be neglected in the Vis and NIR wavelength range, since direct solar radiance is much larger than diffuse radiance. However, due to the strong wavelength dependence of the Rayleigh scattering, the diffuse-light fraction becomes critical at shorter wavelengths and larger solar zenith angles (SZAs) (McKenzie & Johnston, 1995; Slusser et al., 2000; Tüg & Baumann, 1994). The most dominant source of OOF stray light at UV wavelength is diffuse light, since the light path inside the instrument is well sealed from the collimator to the spectrometer. Several main trace gas absorption bands are in UV wavelengths shorter than 360 nm as shown in Figure 1a (e.g., O_3, SO_2, and HCHO). The same is true for important chemical processes of reactive trace gases (e.g., ozone) that occur in the early morning and late afternoon, when SZAs are large (e.g., Crutzen, 1970; Jacob, 2000). Therefore, it is necessary to accurately measure radiances at large SZA and short wavelengths and to reduce error caused by OOF stray light.

To understand diffuse-light contributions to the measurements, we calculated diffuse and direct intensity within the FOV (i.e., 2.2°) using the VLIDORT (linearized pseudo-spherical vector discrete ordinate radiative transfer code; Spurr, 2006) with known (or retrieved) ozone amounts. The fraction of direct and diffuse light in the FOV from calculations is relatively accurate compared to its absolute value. The diffuse-light contribution was corrected by multiplying by the diffuse-light correction factor (DCF) as follows:

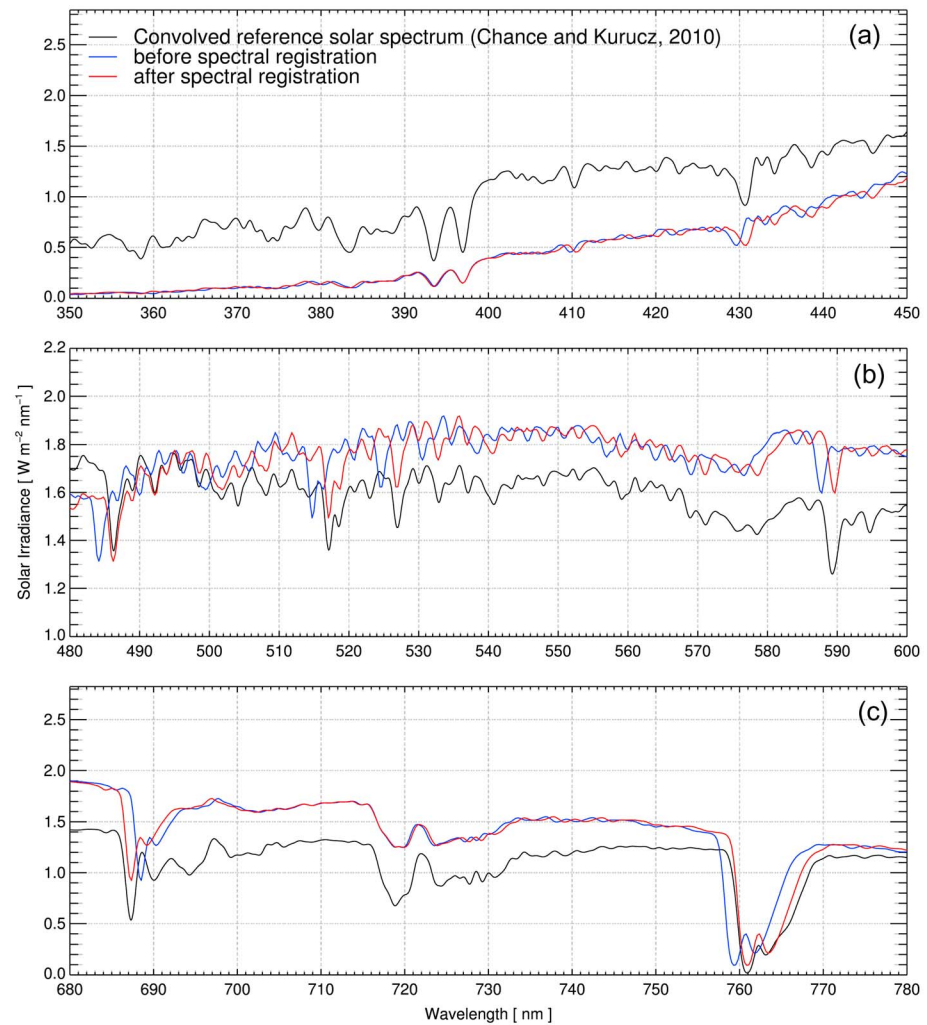$$C_{cor} = \frac{I_{dir}}{I_{dir} + I_{dif}} C, \qquad (4)$$

Figure 2. Wavelength registration results using a nonlinear least squares method at (a) 350–450, (b) 480–600, and (c) 680–780 nm. The black line represents theoretical bottom of the atmosphere irradiance. The blue and red lines represent arbitrarily scaled measurements before and after spectral registration, respectively.
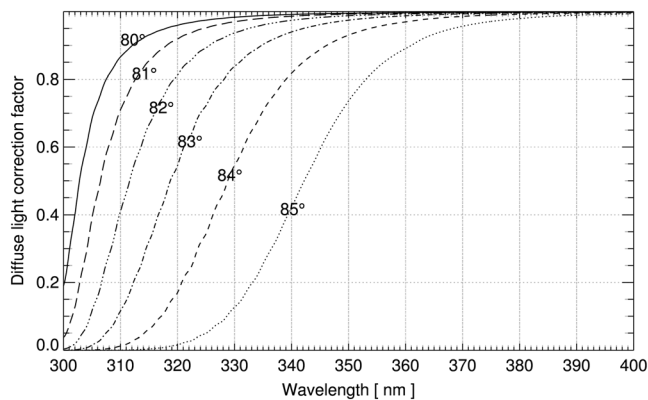

Figure 3. Spectral diffuse-light correction factors of the UV-Vis-NIR spectro-radiometer direct Sun measurements at UV (300–400 nm) wavelength range calculated using VLIDORT with 300 Dobson unit of O_3 and without aerosols and clouds.

where C and C_{cor} are the measured voltage counts before and after the diffuse-contribution correction, respectively. $I_{dir}/(I_{dir} + I_{dif})$ is the DCF, where I_{dir} and I_{dif} are the theoretical direct and diffuse FOV radiances from VLIDORT. An example of calculated DCF in the UV at SZA between 80 and 85° with 300 Dobson units of O_3 vertical column is shown in Figure 3. The diffuse-light contribution increases as SZA increases and wavelength decreases. For example, the diffuse-light incident in the FOV at 300 nm is about 4 times larger than the direct solar light at SZA of 80°, which is the upper limit requirement to minimize the diffuse-light error for aerosol retrieval in this study. Meanwhile, at 330 nm, the DCF is larger than 0.97 at SZA of 80°, which implies that the diffuse-light contribution to measurements is less than 3%. We assumed that the accuracy in the DCF at wavelengths longer than 330 nm and for SZA smaller than 80° is acceptable, since the diffuse-light fraction is relatively low (i.e., less than 3% in this study). These retrieval limitations can be relaxed by calculating diffuse light more precisely, when accurate information on surface, aerosols,
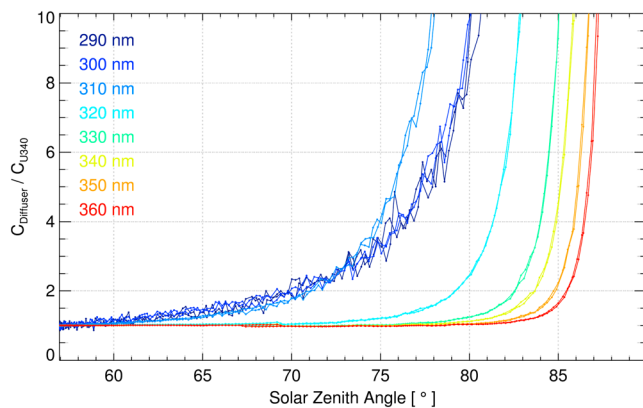
Figure 4. Voltage count ratio of diffuser filter to U340 filter as a function of solar zenith angle at several ultraviolet wavelengths on 12 November 2017. The ratios were normalized to each value at the smallest solar zenith angle (~57°).

and O_3 amounts is available. In addition, the DCF calculation requires further trace gas information such as NO_2 or HCHO concentration, since diffuse-light contribution becomes significant at wavelength up to 390 nm when SZA is 85°. Note that the calculated DCF has spectral high-frequency structures along the strong gas absorption lines (O_3 in Figure 3). Therefore, the DCF is also important for accurate O_3 and SO_2 retrievals at large SZA.

3.5. Out-Of-Band (OOB) Stray Light Correction

Stray light within the instrument, which is unintended light incident on the detector by scattering, reflection, and refraction, is an inherent limitation of the grating system. Prior studies have suggested various OOB stray light correction methods using monochromatic light sources (e.g., Feinholz et al., 2012; Zong et al., 2006). The stray light coming from OOB can cause significantly large errors when the incoming light to a detector is relatively low, compared to the light reaching OOB detectors (Zong et al., 2006). UV measurements using UV-Vis spectrometers have suffered from OOB stray light for this reason, since visible photons in the atmosphere are typically several orders of magnitude greater than UV photons. The UV CCD detectors are typically several hundred detectors away from those at the peak of the visible light. Therefore, characterizing a spectrometer's slit scattering function (the relative spectral responsivity of the instrument spectrometer optics and detector) for the whole detector range is important to correct OOB stray light in the UV wavelengths. However, iterative deconvolution methods using the slit scattering function may not converge to the correct solution, since the practical characterization data have limited accuracy at OOB detectors with low-level counts (detectors far from the in-band detector; e.g., Zong et al., 2006). The current Pandora data processing algorithm first removes OOB stray light from wavelengths longer than 380 nm by using U340 filter for ozone retrieval. Based on the assumption that the incident sunlight at the sea level is nearly zero at wavelengths shorter than 290 nm, the remaining stray light is corrected using the "dark pixel" method, which subtracts the mean signal on the detector at these wavelength positions (Herman et al., 2015; Tzortziou et al., 2012). Following these two-step stray light corrections, empirical measure of uncorrected stray light remains that is as a function of air mass (Herman et al., 2015).

As we use the diffuser filter for broad spectral range τ_{aer} retrievals, the measurements can more suffer from OOB stray light in the UV wavelengths compared to the U340 filter measurements. A more sophisticated stray light correction algorithm with full slit scattering function measurements using a tunable laser should improve the measurement accuracy and will be developed in a future study. In the present study, we empirically estimated OOB stray light coming from far pixels (mainly from Vis to UV) using a simple slit scattering function model. Since the U340 filter rejects most of the visible wavelengths longer than 380 nm, U340 measurements are less affected by the OOB stray light compared to those of diffuser measurements (see Figure 1b). At wavelength shorter than 380 nm, the difference between OOB stray light of the two filter measurements depends on the amount of the light filtered by the U340 filter. On a clear day, we assume that incoming radiances of sequential U340 and diffuse measurements are almost identical, since they typically have a time difference of 1 min or less. At these times, the ratio of consecutive U340 and diffuser filter measurements are expected to equal the ratio of the transmittances of those filters without OOB stray light. However, measured ratios between the two filters were found to be a strong function of SZA due to the diurnal variations of OOB stray light for different filters (Figure 4). The ratios in Figure 4 were normalized to each value at the smallest SZA (~57°). At large SZAs, UV photons direct from the Sun are more effectively scattered compared to visible photons, which leads to a greater fraction of OOB stray light in UV measurements from the diffuser compared to the U340 filter. When this tendency is predictable and consistent, the OOB stray light can be estimated with a best guess slit scattering function model. The slit scattering function of the spectrometer was assumed to be the inverse power of the pixel-distance from in-band detector in this study. The voltage counts measured by the spectroradiometer can be expressed as follows:

$$C(\lambda) = a(\lambda)T(\lambda)I(\lambda) + \sum_{i}^{OOB} \frac{a_i T_i I_i}{(\Delta d_i)^p} \tag{5}$$
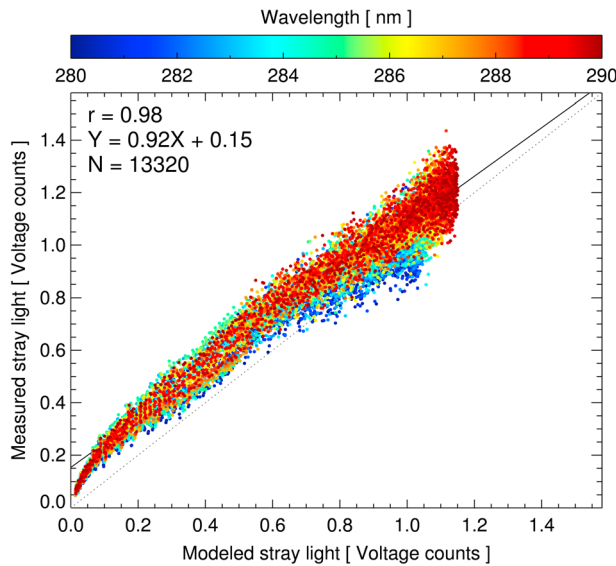
Figure 5. Comparison of modeled (*x* axis) and measured (*y* axis) out-of-band stray light differences between diffuser and U340 filter measurements at wavelengths shorter than 290 nm. The colors of the plots represent wavelengths.

where $C(\lambda)$ is the UV-Vis-NIR spectroradiometer voltage counts at wavelength λ. The first term on the right-hand side of equation (5) is the responsivity to the true signal; a is the gain of spectroradiometer, T is the transmittance of the optics from the collimator to the CCD, and I is the incoming radiance to collimator. The second term on the right-hand side of equation (5) is the OOB stray light term, which is the summation of the stray light from OOB detectors. The Δd_i is the detector distance of the ith OOB detector from the in-band detector, and p is the empirically determined inverse power of the slit scattering model. For wavelengths shorter than 290 nm, most of the recorded counts can be regarded as stray light since actual radiance is much smaller than measurement errors. Under this assumption, equation (6), below, can be derived using equation (5) for the diffuser and U340 filter, where the subscripts D and U denote diffuser and U340, respectively.

$$C_D(\lambda) - C_U(\lambda) \cong \sum_i^{OOB} \frac{a_i T_{D,i} I_i}{(\Delta d_i)^p} - \sum_i^{OOB} \frac{a_i T_{U,i} I_i}{(\Delta d_i)^p}. \qquad (6)$$

The left-hand side of equation (6) is the difference in spectral measurements from the diffuser and U340 mode at wavelengths shorter than 290 nm, which represents the measured OOB stray light difference. The right-hand side is the modeled OOB stray light difference. When the slit scat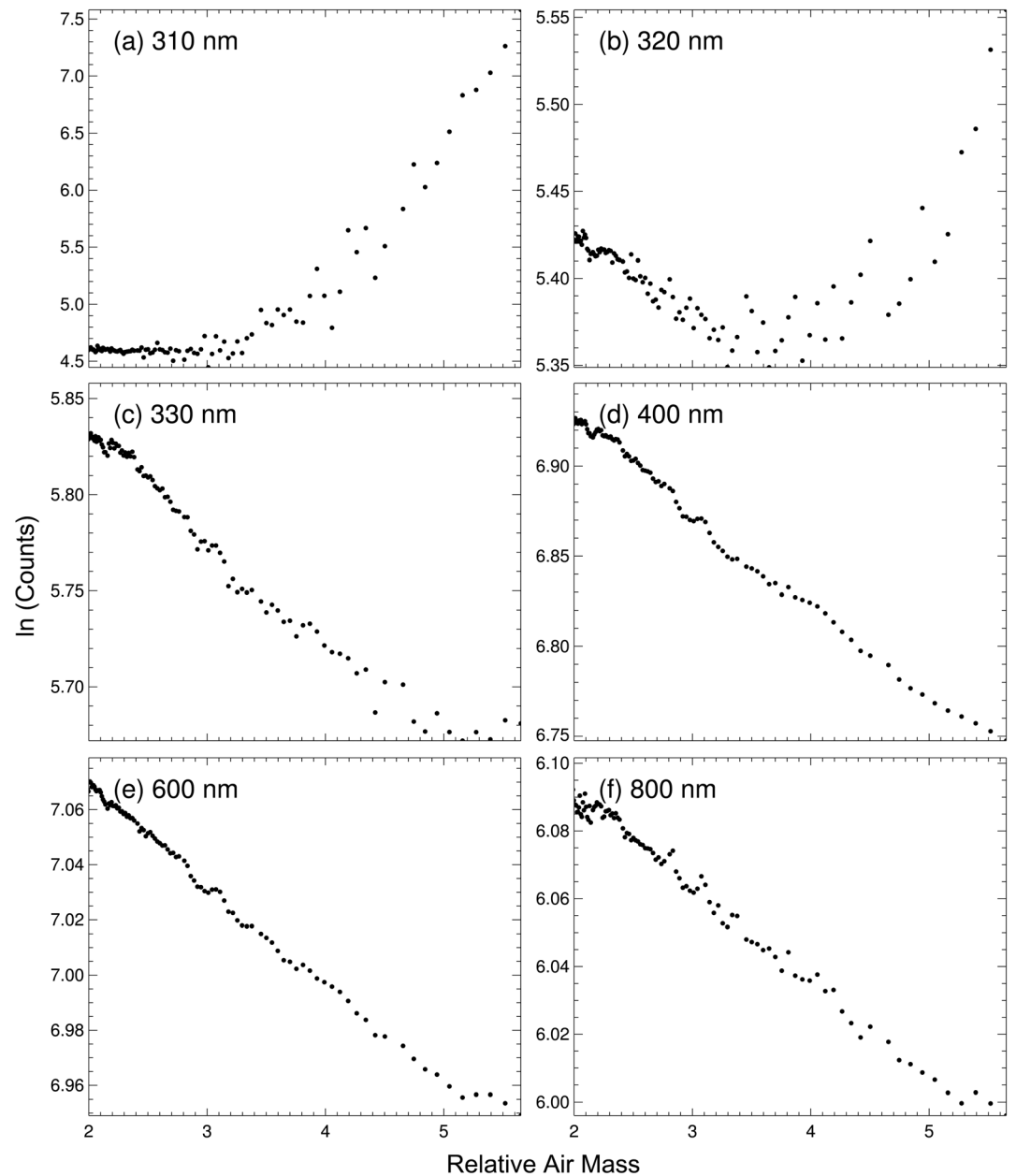tering function model well represents the actual characteristics of the UV-Vis-NIR spectroradiometer, the modeled OOB stray light is expected to agree closely with the measured stray light in equation (6). The p was obtained by iteratively and empirically using the relationship between the two terms at various values (2.09 in this study). The comparison between modeled and measured stray light with the final p is shown in Figure 5. The modeled OOB stray light agrees well with the measured stray light (correlation coefficient = 0.98). The nonlinearity and small offset in Figure 5 may be caused by uncertainties in the inverse power model. Lower agreements might also exist in other units with larger wavelength dependency for the same reason. In those cases, alternative, improved slit scattering function models should be developed. For the current unit, the OOB stray light was corrected by subtracting the modeled OOB stray light from the original measurements. The effects of empirical stray light correction are discussed in section 4. Note that the empirical stray light correction algorithm mainly aims to estimate OOB stray light in the UV wavelengths coming from visible light (far from in-band). We utilized measured near in-band slit scattering function to convolute gas absorption cross sections for spectral fitting.

3.6. Spectral Langley Calibration

The Langley calibration method is based on the B-B-L law and provides inferred measurements of irradiance at TOA and atmospheric attenuation at the measured wavelength (Langley, 1881). Major error sources of the Langley calibration include uncertainties in the calculation of the optical air mass, atmospheric variability, instrument radiometric performance (linearity, offset correction, and stray light), and atmospheric inhomogeneity (e.g., Shaw, 1982, 1983; Slusser et al., 2000; Thomason et al., 1983). Due to the vertical inhomogeneity of the scatterers, different air masses can lead to nonlinear biases in the Langley plot (Thomason et al., 1983). Equation (1) can be reformulated for the Langley calibration to separate species with different relative air masses and to reduce such errors (equation (7); Cheymol & Backer, 2003; Kirchhoff et al., 2001; Thomason et al., 1983). The equation is given by

$$\ln C(\lambda) + m_{Ray}(\lambda)\tau_{Ray}(\lambda) + \sum_i m_i(\lambda)\tau_i(\lambda) = \ln C_0(\lambda) - m_{aer}(\lambda)\tau_{aer}(\lambda), \qquad (7)$$

where C is the measured counts and m_{Ray} and τ_{Ray} are the relative air mass and optical thickness of the Rayleigh scattering, respectively. The m_i and τ_i are the relative air mass and optical thickness of the ith atmospheric gas. C_0 is the virtual count measured at TOA, which can be obtained from the Langley calibration, and m_{aer} and τ_{aer} are the relative air mass and optical thickness of the aerosol. The τ_{Ray} was calculated from the surface pressure, and absorption optical thicknesses of the gases (τ_{gas}) can be obtained from their vertical

Figure 6. Examples of Langley plots using the UV-Vis-NIR direct-Sun measurements on 12 November 2016 at (a) 310, (b) 320, (c) 330, (d) 400, (e) 600, and (f) 800 nm. Positive slope appears in the Langley plots at wavelengths shorter than 320 nm due to uncorrected measurement errors, mostly from stray light. Langley plots at longer wavelengths showed more stable results.

column density retrievals. The relative air mass can be expressed as the following equation, which can be obtained from the Snell's law of refraction for spherical geometry (e.g., Thomason et al., 1983):

$$m = \sec\left\{ \sin^{-1}\left[\left(\frac{r}{r + h_{\text{eff}}}\right) \sin(\text{SZA}^*) \right] \right\}, \tag{8}$$

where r is the distance from the center of the Earth to the measurement location (~6,356.8 km), SZA* is the apparent SZA (i.e., the true SZA corrected for refraction), and h_{eff} is the assumed effective height of a species. The h_{eff} of the aerosols, ozone absorption, and Rayleigh scattering were assumed to be 2.0, 20.4, and 6.2 km,
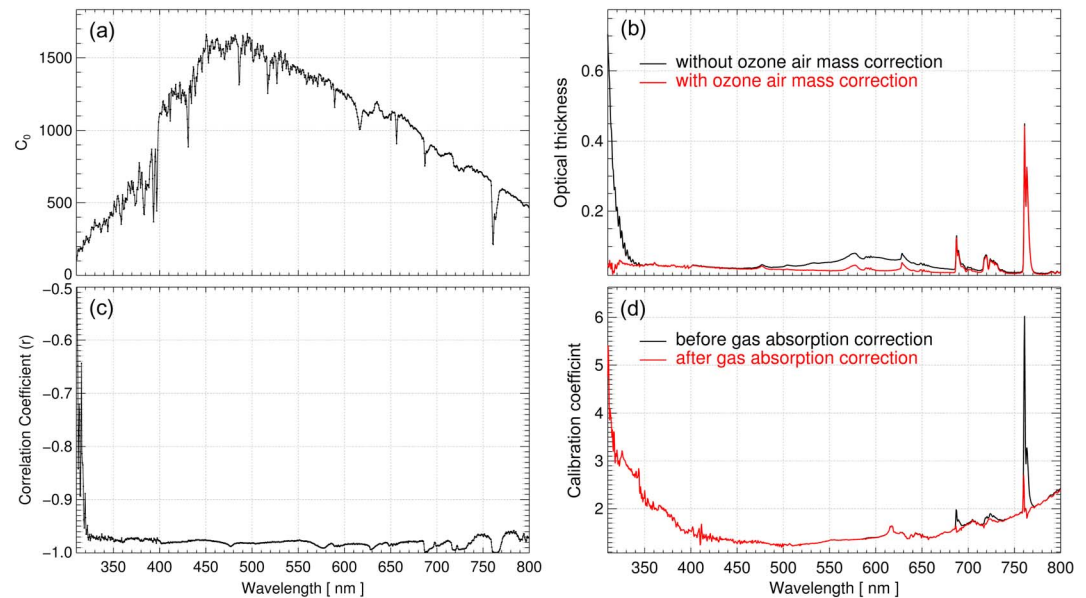
Figure 7. (a) Inferred top of the atmosphere (TOA) voltage count, (b) spectral optical thickness, and (c) correlation coefficients from the Langley calibration on 12 November 2016. (d) Spectral Langley calibration coefficients (TOA solar irradiance divided by TOA voltage count in units of [$mW \cdot m^{-2} \cdot nm^{-1} \cdot counts^{-1}$]) before (black) and after (red) the gas absorption correction.

respectively. Ozone is a major error source for relative air mass calculation, since it is mostly distributed in the stratosphere and is optically thick in its absorption bands. However, since spectroradiometric measurements provide accurate optical thickness of ozone from the gas retrieval algorithm (Herman et al., 2015), it can be corrected by including ozone in the left-hand side of equation (7).

Prior studies using the Langley method mostly used monochromatic light or several discrete channels as input (e.g., Cheymol & Backer, 2003; Kirchhoff et al., 2001). In this study, we performed a Langley calibration at continuous wavelengths from 310 to 800 nm interpolated to a 0.5-nm resolution grid, which covers all major trace gas absorption structures within that range. We used a relatively small relative air mass range (less than 4.0) to ensure the presence of sufficient UV photons so that OOB stray light can be reduced. Examples of Langley plots at several wavelength ranges on 12 November 2016 are shown in Figure 6. Whole spectrum TOA counts, optical thicknesses, correlation coefficients, and calibration constants (solar irradiance divided by TOA counts) from the Langley calibration are shown in Figure 7. Despite our laboratory and field calibration efforts, measurements within the short UV region still suffer from relatively large measurement errors (i.e., correlation coefficients of the Langley plots far from −1.0). Positive slope appears in Langley plot at 310 and 320 nm at large relative air masses due to uncorrected measurement errors, mostly from stray light, as shown in Figures 6a and 6b. This leads to a rapid decrease in optical thickness and increase in correlation coefficient at wavelengths shorter than 325 nm (Figures 7b and 7c). Langley plots at longer wavelengths showed more stable results. The spectral optical thicknesses showed the expected combination of spectrally smooth components and gas absorption structures above about 325 nm as shown in Figure 7b. Note that without ozone air mass correction (by equation (7)), strong features of the ozone Huggins (310–350 nm) and Chappuis band (500–680 nm) appeared in spectral optical thickness. This phenomenon has been previously described in prior studies (e.g., King & Byrne, 1976). However, these features are removed by correcting ozone air mass as shown in Figure 7b. The spectral correlation coefficients were also close to −1 at wavelengths longer than 325 nm as shown in Figure 7c. As the aerosol property retrievals require reliable radiometric calibration, we used the wavelength range from 330 to 800 nm in this study.

The spectral calibration constants are expected to be smooth as a function of wavelength since most bad detectors are filtered out during the calibration procedure. However, structures along strong gas absorption bands (e.g., oxygen and water vapor) still appear in the spectral calibration constants, which might be caused by the temporal variabilities of atmospheric turbidity during the Langley calibration (black line in Figure 7d).
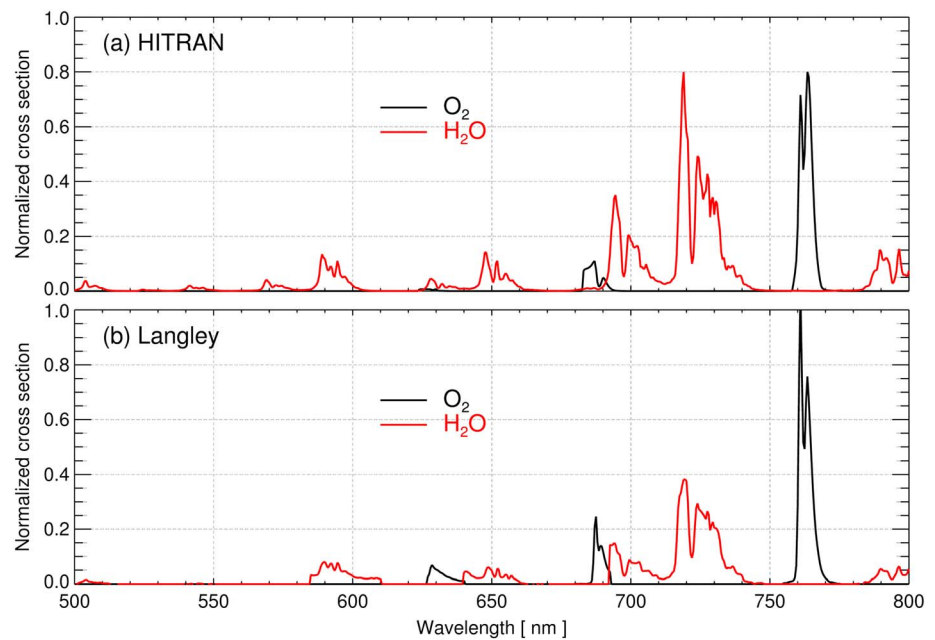
Figure 8. Spectral absorption shape of O_2 and H_2O from (a) HITRAN and (b) spectral optical thickness of Langley calibration result. Note that the plots are normalized to a similar scale to compare their spectral shapes.

These gas absorption features were separated and then subtracted from the original values using a least squares method. The spectral Langley calibration constants before and after gas absorption correction are shown in Figure 7d. This partly compensates for the uncertainties in the Langley calibration constants due to atmospheric variability.
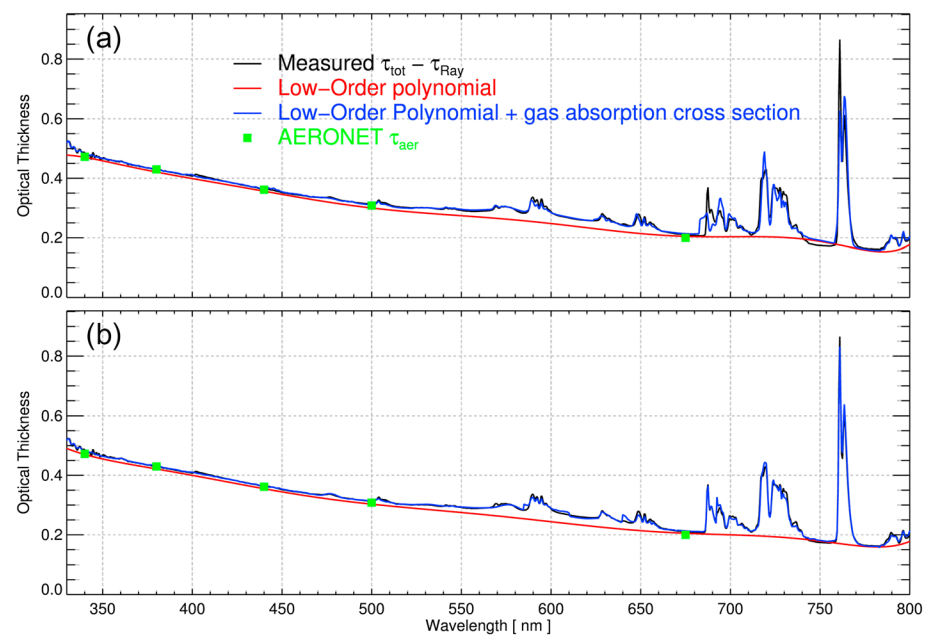
Figure 9. Comparison of least squares fitting results for optical thickness from UV-Vis-NIR spectroradiometer using different sources of absorption cross section. Results in panels (a) and (b) used absorption cross-section of O_2 and H_2O from HITRAN and optical thickness of Langley calibration, respectively. Aerosol optical thickness of AERONET is also shown for comparison as green squares.
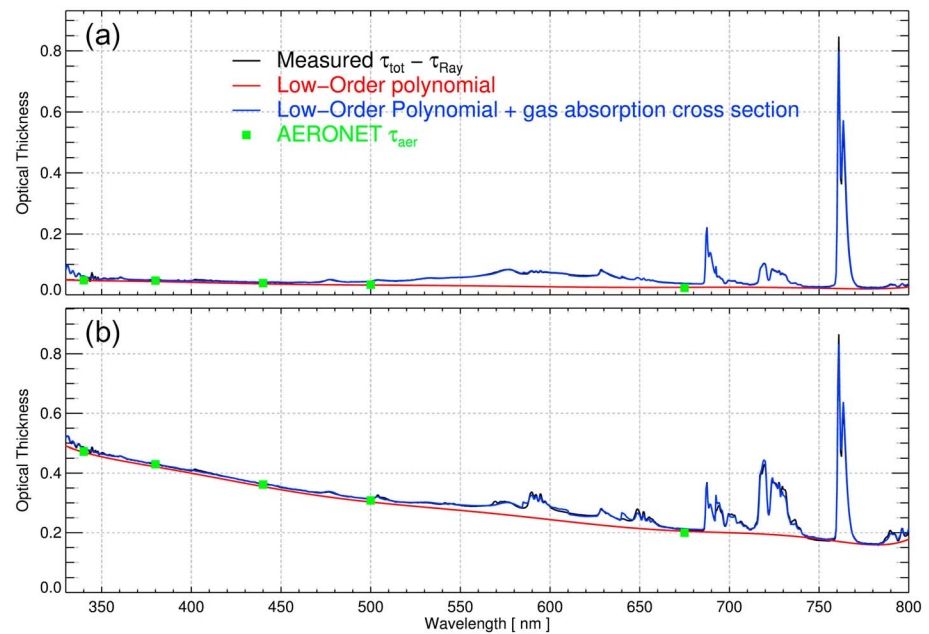
Figure 10. Least squares fitting results of retrieved optical thickness for (a) a clear case (12 November 2016) and (b) a moderate aerosol loading case (20 October 2016). Aerosol optical thickness of Aerosol Robotic Network (AERONET) is also shown for comparison as green squares.

4. Retrieval of Spectral Aerosol Optical Thickness

The τ_{Ray} was calculated from surface pressure data and then subtracted from total optical thickness (τ_{tot}) obtained from C^{λ} and $C_0{}^{\lambda}$. When cloud measurements are successfully screened out, the remaining optical thickness can be regarded as the sum of τ_{gas} and τ_{aer}. Unlike monochromatic or discrete spectral measurements, the UV-Vis-NIR spectroradiometer provides continuous spectral optical thicknesses, which can be more easily separated into spectral high- and low-frequency components. The spectral high-frequency components are mostly associated with the absorption by gases, whereas low-frequency components include information on other atmospheric species, including aerosols and clouds. The τ_{tot} was separated into gas absorption optical thicknesses and combination of low-order polynomials using spectral fitting based on a least squares method that minimizes the following cost function:

$$\chi^2 = \int \left[\tau(\lambda) - \left\{ \sum_{i=0}^{n} P_i \lambda^i + \sum_j K_j \sigma_j(\lambda) \right\} \right]^2 d\lambda \qquad (9)$$

where τ is the total optical thickness minus τ_{Ray} and P and K are the regression coefficients of low-order polynomials and trace gas absorption, respectively. The σ is the absorption cross section of atmospheric gases convolved by the spectrometer slit function. An insufficient number of polynomials can dilute the spectral features of τ_{aer}, whereas too many can over fit the gas absorption components. During the three-month study period, the number of polynomials was not significantly sensitive to spectral τ_{aer} retrievals when the utilized polynomials are between about 5–15. The number of polynomials representing the low-frequency component was determined empirically at the middle of those numbers of polynomials (10 in this study) to secure as much information of spectral features of τ_{aer} as possible and to reduce contamination by trace gas absorption features.

Discrepancies in spectral gas absorption between actual optical thickness measurements (i.e., τ_{tot}) and known (or theoretical) databases can produce fitting residuals. This is typically caused by the uncertainties in the characterized slit function of the instruments or the absorption cross sections of the gases. Such differences were found mostly for O_2 and H_2O since they have sharp and strong absorption bands. The fitting error can then propagate into the errors in the spectral τ_{aer} retrieval. In order to reduce such uncertainties, we used
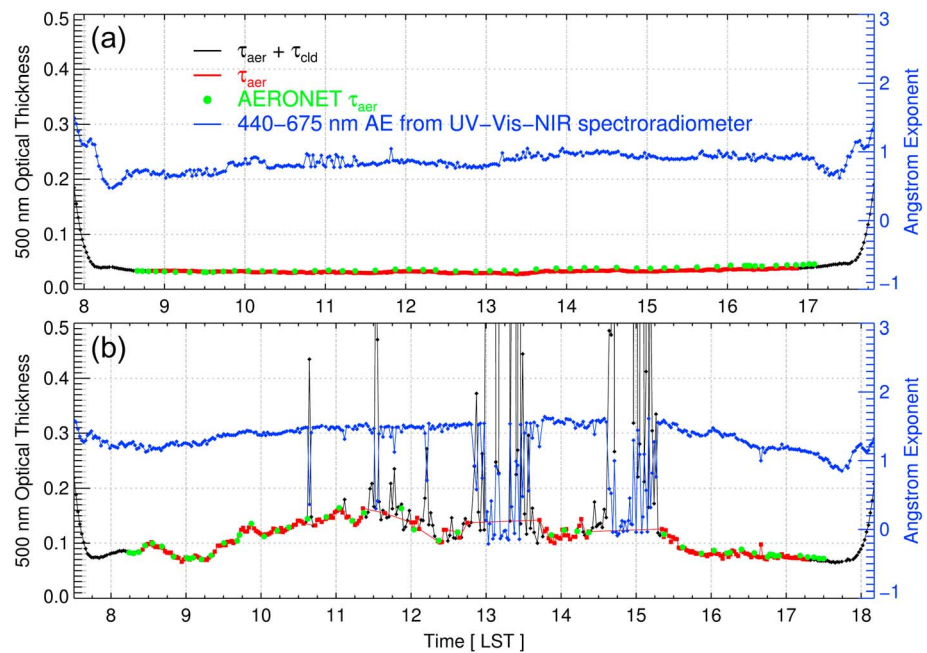
Figure 11. Temporal variations of aerosol and cloud optical thickness at 500 nm and Ångström Exponent (AE) on (a) a clear day (12 November 2016) and (b) a partly cloudy day (23 October 2016). Early morning and late afternoon data were screened out by retrieval criteria of solar zenith angle (80°).

the spectral absorption shape of H_2O and O_2 in the Langley plot in Figure 7b. The spectral absorption shape of H_2O and O_2 from HIgh-resolution TRANsmission molecular absorption database (HITRAN; Rothman et al., 2013) and Langley optical thicknesses are compared in Figure 8. Note that the absolute values in Figure 8 are not relevant, since only the shape of spectral gas absorption is used for spectral fitting. Even though their general spectral absorption shapes are similar, there are differences in their specific structures, particularly in the O_2-A (around 765 nm) and O_2-B (around 685 nm) absorption bands. Those differences can cause nonnegligible uncertainties of spectral τ_{aer} retrievals. Spectral fitting results using HITRAN and Langley calibration gas absorption shape are compared in Figures 9a and 9b, respectively. Large fitting residuals near O_2 and H_2O absorption bands in Figure 9a are considerably reduced in Figure 9b (typically factor of 2–3 for whole spectral range), leading to different τ_{aer} retrievals (red lines). Therefore, characterizations of more accurate atmospheric gas absorption cross sections and slit function of instruments are important for both the trace gases and aerosol retrievals by separating each contribution to the τ_{tot}.

Examples of the separation of the τ_{gas} and τ_{aer} using a linear least squares method for low (12 November 2016) and moderate aerosol loading (20 October 2016) cases are shown in Figures 10a and 10b, respectively. The results across all retrieved spectral τ_{aer} show generally in good agreement with those from AERONET for both cases. The spectral features of τ_{aer} are traditionally analyzed using the Ångström Exponent (AE) at discrete channels, which is related to the size of the particles. The continuous spectrum of τ_{aer} from UV-Vis–NIR spectroradiometer is expected to provide more informative constraints for additional aerosol property retrievals using diffuse-sky measurements. It also enables application of higher-order derivatives and spectrally high-resolution inversion methods to the measurements (e.g., Hansell et al., 2014).

Figure 11 compares the diurnal variations of τ_{aer} at 500 nm retrieved in this study and those from AERONET on (a) a clear day (12 November 2016) and (b) a partly cloudy day (23 October 2016). AE between 440 and 675 nm is also plotted to compare temporal variations with those

Table 2
Aerosol Retrieval Condition Screening Parameters and Their Criteria

Screening parameter	Criterion
AE (440–675 nm)	>0
σ_τ[a]/σ_{time}[b]	<0.005
σ_{AE}[c]/σ_{time}	<0.07
Solar zenith angle	$<80°$

[a]Standard deviation of the five-consecutive optical thickness measurements at 500 nm. [b]Standard deviation of the five-consecutive measurement time in minutes. [c]Standard deviation of the five-consecutive Ångström Exponent between 440 and 675 nm.
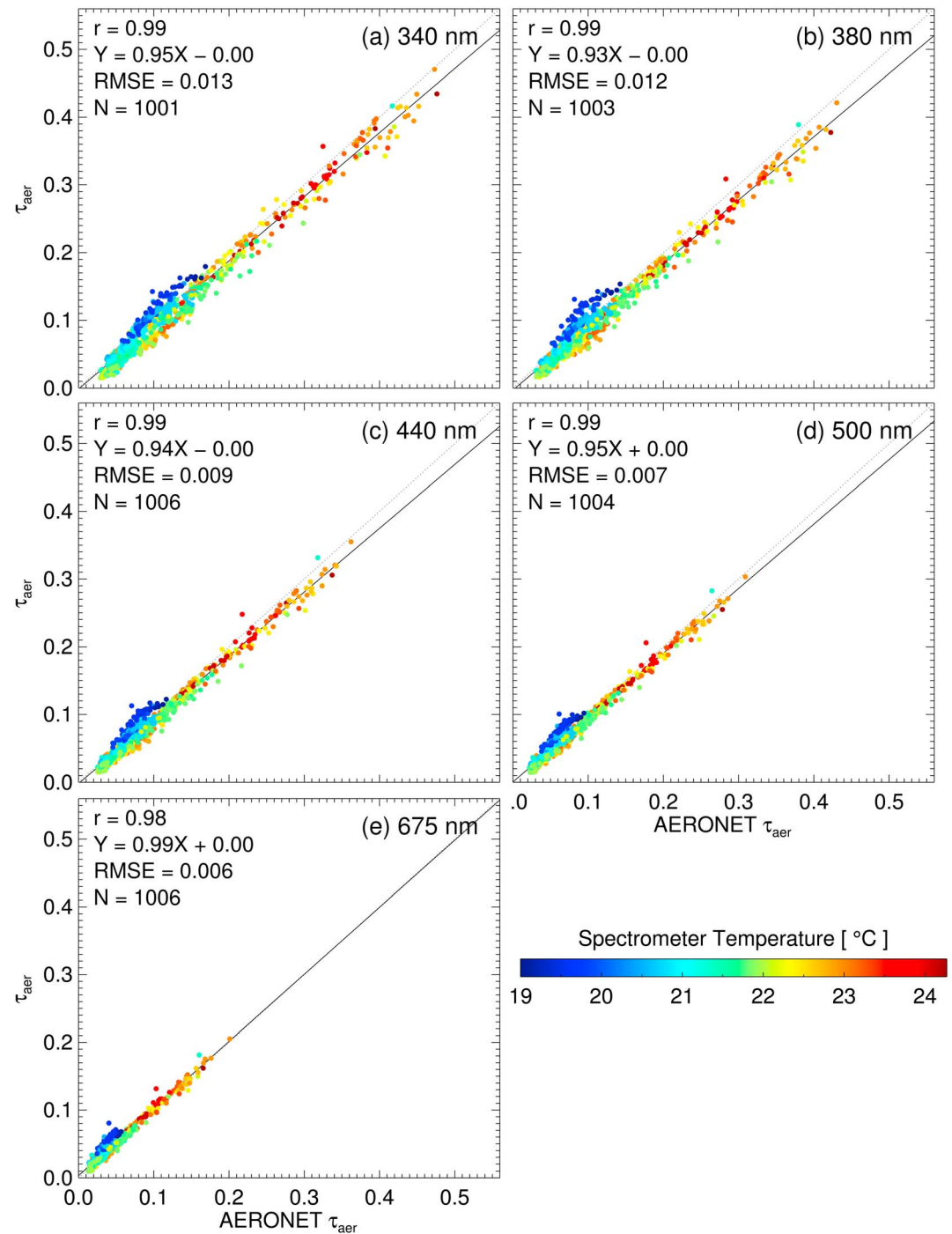

Figure 12. Intercomparison of retrieved aerosol optical thickness from ultraviolet-visible-near-infrared spectroradiometer and Aerosol Robotic Network (AERONET) at (a) 340, (b) 380, (c) 440, (d) 500, and (e) 675 nm. The color of the scatter plot points represents the temperature of the spectrometer.

of τ_{aer} and cloud optical thickness (τ_{cld}). As shown in Figure 11b, abrupt increases in optical thickness and decreases in AE were found when the measurements were contaminated by clouds, due to their relatively large optical thickness and size. Since clouds typically have larger spatial variability compared to aerosols, temporal variations in τ_{cld} and AE are also much larger than those of aerosols as the clouds pass over the FOV. The aerosol retrieval condition parameters and their criteria were determined empirically based on
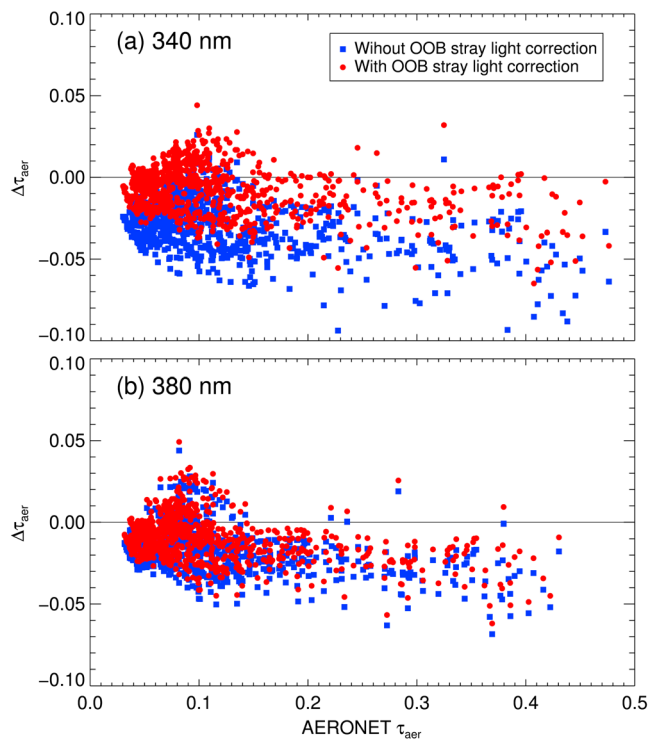
Figure 13. The difference of retrieved aerosol optical thickness ($\Delta\tau$, ultraviolet-visible-near-infrared spectroradiometer-Aerosol Robotic Network [AERONET]) as a function of AERONET measurements at (a) 340 and (b) 380 nm. The blue squares and red circles represent before and after out-of-band stray light correction, respectively. The empirical stray correction algorithm has a significant impact on retrievals at shorter wavelengths (340 nm).

the characteristics as listed in Table 2. The sum of τ_{aer} and τ_{cld} (before cloud screening) is plotted in the black line, whereas the cloud-screened τ_{aer} is shown in the red line. After the clouds are successfully filtered out, τ_{aer} shows good agreement with the AERONET product as shown in Figure 11b. This also demonstrates the possibility of retrieving τ_{cld} and other optical properties of thin clouds. Since the cloud effects on trace gas retrievals are also important, they will be investigated in a future study.

Retrieved spectral τ_{aer} overlapping those from AERONET channels during the period from 20 October 2016 to 19 January 2017 are compared in Figure 12. Note that the numbers of data points in each panel differ since AERONET provides a different number of retrievals for each channel after data-quality-assurance-processing. The color of the scatter plot points represents the temperature of the spectrometer, which affects the radiometric calibration constants of the whole spectroradiometer system. Spectral τ_{aer} from the UV-Vis-NIR spectroradiometer and AERONET showed good agreements at all wavelengths (correlation coefficients greater than 0.98). The root-mean-squared-error values were within known uncertainty level of AERONET at all wavelengths (i.e., 0.02 at UV and 0.01 at visible channels) (Eck et al., 1999). The low slopes (0.93–0.99) are due to UV-Vis-NIR spectroradiometer's relative underestimation of radiance at high optical depths and relative overestimation at low optical depths, which might be a function of the spectrometer temperature. However, it also could be caused by other factors that are correlated with the spectroradiometer temperature variation or uncertainties in AERONET measurements. Therefore, no further corrections for temperature sensitivity of the radiometric calibration constants were applied in this study. Further temperature-dependent radiometric calibrations in a well-controlled laboratory experiment are necessary to identify actual temperature effects and thereby improve the τ_{aer} retrievals.

OOB stray light at shorter wavelengths was also observed by early AERONET measurements under high-turbidity conditions (Smirnov et al., 2000). However, AERONET successfully screened out the contaminated scenes by rejecting low measurement signals (i.e., less than 50 voltage counts). Furthermore, utilizing ion-assisted deposition filters significantly improved OOB stray light blocking for the shortwave measurements (Smirnov et al., 2000). Therefore, OOB stray light effects of the AERONET data should be relatively small compared to the uncorrected data of the UV-Vis-NIR spectroradiometer. The effects of the empirical stray light correction algorithm developed in this study are displayed in Figure 13, which shows biases of retrieved τ_{aer} at 380 and 380 nm between UV-Vis-NIR spectroradiometer and AERONET before and after stray light correction. Since the contribution of stray light is critical in the shorter UV, we observe meaningful improvements with stray light correction at 340 nm, whereas we obtain relatively smaller effects at 380 nm. Effects of empirical OOB stray correction were even smaller or negligible at longer wavelengths.

5. Summary and Conclusions

A spectral (330–800 nm) retrieval algorithm of τ_{aer} based on the Langley calibration method for direct-Sun UV-Vis-NIR spectroradiometer measurements was developed. OOF stray light, due to diffuse-light contribution to the incoming radiances in the FOV, was corrected using theoretical VLIDORT radiative transfer calculations. An empirical stray light correction method was developed using the difference in OOB stray light from U340 and diffuser measurements. Wavelengths of each detector were registered using a nonlinear least squares method with first guess values from lamp calibration. Spectral Langley plots showed good correlation for wavelengths longer than 330 nm; however, they suffered from relatively larger measurement errors and weak signals at wavelength shorter than 320 nm. Uncertainties in the Langley calibration due to

atmospheric variability were partly corrected by removing the gas absorption components in the spectral calibration constants. The τ_{Ray} was estimated using the surface pressure, and then subtracted from τ_{tot}. The remaining optical thickness was separated into a gas absorption component and low-order polynomials using a least squares method. To reduce the fitting residuals, spectral gas absorption shapes from the Langley calibration results were used for H_2O and O_2. Cloud-contaminated measurements were filtered out whenever low AE values or large temporal variations in optical thickness were observed.

The retrieved τ_{aer} showed good agreement with the benchmark AERONET product at all overlapping wavelengths during the measurement period ($r > 0.98$). Slightly lower slopes (0.93–1.0) relative to AERONET might be caused by the temperature sensitivity of the spectrometer, which can be improved by more sophisticated, temperature-dependent radiometric calibrations or a better temperature controller. Empirical stray light correction considerably improved τ_{aer} retrievals of UV-Vis-NIR spectroradiometer radiances at short wavelengths, which is critical for several trace gas retrievals. A more realistic OOB stray light model can improve the performance of the correction algorithm. The UV-Vis-NIR spectroradiometer system has the benefit of measuring τ_{aer} at continuous wavelengths simultaneously, which has been shown to provide useful information on aerosols and reliable spectral dependence. Moreover, a strategic network of these well-calibrated ground-based spectroradiometers would comprehensively complement and aid in validation of spatial and temporal aerosol and trace gas measurements from spaceborne geostationary platforms. Future studies will expand on using spectral τ_{aer} values in conjunction with diffuse and/or polarization measurements for developing retrievals of additional aerosol properties, including aerosol bulk vertical distribution, absorption, and size. These aerosol properties are also important for trace gas profile retrieval algorithms.

References

Bovensmann, H., Burrows, J. P., Buchwitz, M., Frerick, J., Noël, S., & Rozanov, V. (1999). SCIAMACHY: Mission objectives and measurement modes. *Journal of the Atmospheric Sciences*, 56(2), 127–150. https://doi.org/10.1175/1520-0469(1999)056%3C0127:SMOAMM%3E2.0.CO;2

Brion, J., Chakir, A., Charbonnier, J., Daumont, D., Parsse, C., & Malicet, J. (1998). Absorption spectra measurements for the ozone molecule in the 350–830 nm region. *Journal of Atmospheric Chemistry*, 30(2), 291–299. https://doi.org/10.1023/A:1006036924364

Brion, J., Chakir, A., Daumont, D., Malicet, J., & Parisse, C. (1993). High-resolution laboratory cross-sections of O_3: Temperature effect. *Chemical Physics Letters*, 213(5-6), 610–612. https://doi.org/10.1016/0009-2614(93)89169-I

Burrows, J. P., Weber, M., Buchwitz, M., Rozanov, V., Ladstätter-Weißenmayer, A., Richter, A., et al. (1999). The global ozone monitoring experiment (GOME): Mission concept and first scientific results. *Journal of the Atmospheric Sciences*, 56(2), 151–175. https://doi.org/10.1175/1520-0469(1999)056%3C0151:TGOMEG%3E2.0.CO;2

Casper, C., & Chance, K. (1997). GOME wavelength calibration using solar and atmospheric spectra, Proc. 3rd ERS Symp. On space at the service of our environment, Florence, Italy, 17–21 March 1997 (ESA SP-414, 3 Vols., May 1997).

Chance, K., & Kurucz, R. L. (2010). An improved high-resolution solar reference spectrum for Earth 's atmosphere measurements in the ultraviolet, visible, and near infrared. *Journal of Quantitative Spectroscopy and Radiative*, 111(9), 1289–1295. https://doi.org/10.1016/j.jqsrt.2010.01.036

Chance, K., & Orphal, J. (2011). Revised ultraviolet absorption cross sections of H_2CO for the HITRAN database. *Journal of Quantitative Spectroscopy and Radiative*, 112(9), 1509–1510. https://doi.org/10.1016/j.jqsrt.2011.02.002

Cheymol, A., & Backer, H. D. (2003). Retrieval of the aerosol optical depth in the UV-B at Uccle from Brewer ozone measurements over a long time period 1984-2002. *Journal of Geophysical Research*, 108(D24), 4800. https://doi.org/10.1029/2003JD003758

Chimot, J., Vlemmix, T., Veefkind, J. P., de Haan, J. F., & Levelt, P. F. (2016). Impact of aerosols on the OMI tropospheric NO_2 retrievals over industrialized regions: How accurate is the aerosol correction of cloud-free scenes via a simple cloud model? *Atmospheric Measurement Techniques*, 9(2), 359–382. https://doi.org/10.5194/amt-9-359-2016

Crutzen, P. J. (1970). The influence of nitrogen oxides on the atmospheric ozone content. *Quarterly Journal of the Royal Meteorological Society*, 96(408), 320–325. https://doi.org/10.1002/qj.49709640815

Dobovik, O., Holben, B., Eck, T. F., Smirnov, A., Kaufman, Y. J., King, M. D., et al. (2002). Variability of absorption and optical properties of key aerosol types observed in worldwide location. *Journal of the Atmospheric Sciences*, 59(3), 590–608. https://doi.org/10.1175/1520-0469(2002)059%3C0590:VOAAOP%3E2.0.CO;2

Dubovik, O., & King, M. D. (2000). A flexible inversion algorithm for retrieval of aerosol optical properties from Sun and sky radiance measurements. *Journal of Geophysical Research*, 105(D16), 20,673–20,696. https://doi.org/10.1029/2000JD900282

Eck, T. F., Holben, B. N., Reid, J. S., Dubovik, O., Smirnov, A., O'Neill, N. T., et al. (1999). Wavelength dependence of the optical depth of biomass burning, urban, and desert dust aerosols. *Journal of Geophysical Research*, 104(D24), 31,333–31,349. https://doi.org/10.1029/1999JD900923

Feinholz, M. E., Flora, S. J., Brown, S. W., Zong, Y., Lykke, K. R., Yarbrough, M. A., et al. (2012). *Applied Optics*, 51(16), 3631–3641. https://doi.org/10.1364/AO.51.003631

Grassl, H. (1971). Determination of aerosol size distributions from spectral attenuation measurements. *Applied Optics*, 10(11), 2534–2538. https://doi.org/10.1364/AO.10.002534

Greenblatt, G., Orlando, J. J., Burkholder, J. B., & Ravishankara, A. R. (1990). Absorption measurements of oxygen between 330 and 1140 nm. *Journal of Geophysical Research*, 95(D11), 18,577–18,582. https://doi.org/10.1029/JD095iD11p18577

Hansell, R. A., Tsay, S.-C., Pantina, P., Lewis, J. R., Ji, Q., & Herman, J. R. (2014). Spectral derivative analysis of solar spectroradiometric measurements: Theoretical basis. *Journal of Geophysical Research*, 119, 8908–8924. https://doi.org/10.1002/2013JD021423

Herman, J. R., Cede, A., Spinei, E., Mount, G., Tzortziou, M., & Abuhassan, N. (2009). NO_2 column amounts from ground-based Pandora and MFDOAS spectrometers using the direct-Sun DOAS technique: Intercomparisons and application to OMI validation. *Journal of Geophysical Research*, 114, D13307. https://doi.org/10.1029/2009JD011848

Herman, J. R., Evans, A., Cede, N., Abuhassan, I. P., & McConville, G. (2015). Comparison of ozone retrievals from the Pandora spectrometer system and Dobson spectrometer in Boulder, Colorado. *Atmospheric Measurement Techniques*, 8(8), 3407–3418. https://doi.org/10.5194/amt-8-3407-2015

Holben, B. N., Eck, T. F., Slutsker, I., Tanré, D., Buis, J. P., setzer, A., et al. (1998). AERONET-A federated instrument network and data archive for aerosol characterization. *Remote Sensing of Environment*, 66, 1–16.

Hong, H., Lee, H., Kim, J., Jeong, U., Ryu, J., & Lee, D. S. (2017). Investigation of simultaneous effects of aerosol properties and aerosol peak height on the air mass factors for space-borne NO_2 retrievals. *Remote Sensing*, 9(3), 208. https://doi.org/10.3390/rs9030208

Hönninger, G., von Friedeburg, C., & Platt, U. (2004). Multi axis differential optical absorption spectroscopy (MAX-DOAS). *Atmospheric Chemistry and Physics*, 4(1), 231–254. https://doi.org/10.5194/acp-4-231-2004

Ingmann, P., Veihelmann, B., Langen, J., Lamarre, D., Stark, H., & Courreges-Lacoste, G. B. (2012). Requirements for the GMES Atmosphere Service and ESA's implementation concept: Sentinels-4/-5 and -5p. *Remote Sensing of Environment*, 120, 58–69. https://doi.org/10.1016/j.rse.2012.01.023

Intergovernmental Panel on Climate Change (2013). *Contribution of Working Group I to the Fifth Assessment Report of the Intergovernmental Panel on Climate Change*. Cambridge, UK and New York: Cambridge University Press.

Jacob, D. J. (2000). Heterogeneous chemistry and tropospheric ozone. *Atmospheric Environment*, 34(12-14), 2131–2159. https://doi.org/10.1016/S1352-2310(99)00462-8

Ji, Q., & Tsay, S.-C. (2010). A novel nonintrusive method to resolve the thermal dome effect of pyranometers: Instrumentation an observational basis. *Journal of Geophysical Research*, 115, D00K21. https://doi.org/10.1029/2009JD013483

Ji, Q., Tsay, S.-C., Lau, K. M., Hansell, R. A., Butler, J. J., & Cooper, J. W. (2011). A novel nonintrusive method to resolve the thermal dome effect of pyranometers: Radiometric calibration and implications. *Journal of Geophysical Research*, 116, D24105. https://doi.org/10.1029/2011JD016466

Kampa, M., & Castanas, E. (2008). Human health effects of air pollution. *Environmental Pollution*, 151(2), 362–367. https://doi.org/10.1016/j.envpol.2007.06.012

King, M., & Byrne, D. (1976). A method for inferring total ozone content from the spectral variation of total optical depth obtained with a solar radiometer. *Journal of the Atmospheric Sciences*, 33(11), 2242–2251. https://doi.org/10.1175/1520-0469(1976)033%3C2242:AMFITO%3E2.0.CO;2

King, M., Byrne, D., Herman, B., & Reagan, J. (1978). Aerosol size distributions obtained by the inversion of spectral optical depth measurements. *Journal of the Atmospheric Sciences*, 35(11), 2153–2167. https://doi.org/10.1175/1520-0469(1978)035%3C2153:ASDOBI%3E2.0.CO;2

Kirchhoff, V. W. J. H., Silva, A. A., Costa, C. A., Paes Leme, N., Pavão, H. G., & Zaratti, F. (2001). UV-B optical thickness observations of the atmosphere. *Journal of Geophysical Research*, 106(D3), 2963–2973. https://doi.org/10.1029/2000JD900506

Langley, S. P. (1881). The bolometer and radiant energy. *Proceedings of the American Academy of Arts and Sciences*, 16, 342.

Leitão, J., Richter, A., Vrekoussis, M., Kokhanovsky, A., Zhang, Q. J., Beekmann, M., & Burrows, J. P. (2010). On the improvement of NO_2 satellite retrievals—Aerosol impact on the airmass factors. *Atmospheric Measurement Techniques*, 3(2), 475–493. https://doi.org/10.5194/amt-3-475-2010

Levelt, P. F., van den Oord, G. H. J., Dobber, M. R., Mälkki, A., Visser, H., de Vries, J., et al. (2006). The ozone monitoring instrument. *IEEE Transactions on Geoscience and Remote Sensing*, 44(5), 1093–1101. https://doi.org/10.1109/TGRS.2006.872333

Lin, J.-T., Martin, R. V., Boersma, K. F., Sneep, M., Stammes, P., Spurr, R., et al. (2014). Retrieving tropospheric nitrogen dioxide from the Ozone Monitoring Instrument: Effects of aerosols, surface reflectance anisotropy, and vertical profile of nitrogen dioxide. *Atmospheric Chemistry and Physics*, 14(3), 1441–1461. https://doi.org/10.5194/acp-14-1441-2014

Marquardt, D. L. (1963). An algorithm for least-squares estimation of nonlinear parameters. *Journal of the Society for Industrial and Applied Mathematics*, 2, 431.

McKenzie, R., & Johnston, P. V. (1995). Comment on "Problems of UV-B radiation measurements in biological research: Critical remarks on current techniques and suggestions for improvements" by H. Tüg and M. E. M. Baumann. *Geophysical Research Letters*, 22(9), 1157–1158. https://doi.org/10.1029/95GL01115

Munro, R., Lang, R., Klaes, D., Poli, G., Retscher, C., Lindstrot, R., et al. (2016). The GOME-2 instrument on the Metop series of satellites: Instrument design, calibration, and level 1 data processing-an overview. *Atmospheric Measurement Techniques*, 9(3), 1279–1301. https://doi.org/10.5194/amt-9-1279-2016

Rothman, L. S., Gordon, I. E., Babikov, Y., Barbe, A., Chris Benner, D., Bernath, P. F., et al. (2013). The HITRAN2012 molecular spectroscopic database. *Journal of Quantitative Spectroscopy and Radiative*, 130, 4–50. https://doi.org/10.1016/j.jqsrt.2013.07.002

Schotland, R. M., & Lea, T. K. (1986). Bias in a solar constant determination by the Langley method due to structured atmospheric aerosol. *Applied Optics*, 25(15), 2486–2491. https://doi.org/10.1364/AO.25.002486

Shaw, G. E. (1982). Solar spectral irradiance and atmospheric transmission at Mauna Loa Observatory. *Applied Optics*, 21(11), 2006–2011. https://doi.org/10.1364/AO.21.002006

Shaw, G. E. (1983). Sun photometry. *Bulletin of the American Meteorological Society*, 64(1), 4–10. https://doi.org/10.1175/1520-0477(1983)064%3C0004:SP%3E2.0.CO;2

Slusser, J., Gibson, J., Bigelow, D., Kolinski, D., Disterhoft, P., Lantz, K., & Beaubien, A. (2000). Langley method of calibrating UV filter radiometers. *Journal of Geophysical Research*, 105(D4), 4841–4849. https://doi.org/10.1029/1999JD900451

Smirnov, A., Holben, B. N., Eck, T. F., Dubovik, O., & Slutsker, I. (2000). Cloud-screening and quality control algorithms for the AERONET database. *Remote Sensing of Environment*, 73(3), 337–349. https://doi.org/10.1016/S0034-4257(00)00109-7

Spurr, R. J. D. (2006). VLIDORT: A linearized pseudo-spherical vector discrete ordinate radiative transfer code for forward model and retrieval studies in multilayer multiple scattering media. *Journal of Quantitative Spectroscopy and Radiative*, 102(2), 316–342. https://doi.org/10.1016/j.jqsrt.2006.05.005

Thomason, L. W., Herman, B. M., & Reagan, J. A. (1983). The effect of atmospheric attenuators with structured vertical distributions on air mass determinations and Langley plot analysis. *Journal of the Atmospheric Sciences*, 40(7), 1851–1854. https://doi.org/10.1175/1520-0469(1983)040%3C1851:TEOAAW%3E2.0.CO;2

Torres, B., Dubovik, O., Fuertes, D., Schuster, G., Cachorro, V. E., Lapyonok, T., et al. (2016). Advanced characterization of aerosol properties from measurements of spectral optical depth using the GRASP algorithm. *Atmospheric Measurement Techniques Discussions*, 1–47. https://doi.org/10.5194/amt-2016-334

Torres, O., & Bhartia, P. K. (1999). Impact of tropospheric aerosol absorption on ozone retrieval from backscattered ultraviolet measurements. *Journal of Geophysical Research*, 104(D17), 21,569–21,577. https://doi.org/10.1029/1999JD900410

Tsay, S.-C., Maring, H. B., Lin, N.-H., Buntoung, S., Chantara, S., Chuang, H.-C., et al. (2016). Satellite-surface perspectives of air quality and aerosol-cloud effects on the environment: An overview of 7-SEAS/BASELInE. *Aerosol and Air Quality Research*, *16*(11), 2581–2602. https://doi.org/10.4209/aaqr.2016.08.0350

Tüg, H., & Baumann, M. E. M. (1994). Problems of UV-B radiation measurements in biological research. Critical remarks on current techniques and suggestions for improvements. *Geophysical Research Letters*, *21*(8), 689–692. https://doi.org/10.1029/94GL00373

Tzortziou, M., Herman, J. R., Cede, A., & Abuhassan, N. (2012). High precision, absolute total column ozone measurements form the Pandora spectrometer system: Comparisons with data from a Brewer double monochromator and Aura OMI. *Journal of Geophysical Research*, *117*, D16303. https://doi.org/10.1029/2012JD017814

Vandaele, A. C., Simon, P. C., Guilmot, J. M., Carleer, M., & Colin, R. (1994). SO2 absorption cross section measurement in the UV using a Fourier transform spectrometer. *Journal of Geophysical Research*, *99*(D12), 25,599–25,605. https://doi.org/10.1029/94JD02187

Wagner, T., Beirle, S., Deutschmann, T., Eigemeier, E., Frankenberg, C., Grzegorski, M., et al. (2008). Monitoring of atmospheric trace gases, clouds, aerosols and surface properties from UV/Vis/NIR satellite instruments. *Journal of Optics A: Pure and Applied Optics*, *10*(10), 104019. https://doi.org/10.1088/1464-4258/10/10/104019

Welton, E. J., Campbell, J. R., Spinhirne, J. D., & Scott, V. S. (2001). Global monitoring of clouds and aerosols using a network of Micro-Pulse Lidar systems. In U. N. Singh, T. Itabe, & N. Sugimoto (Eds.), *Lidar Remote Sensing for Industry and Environmental Monitoring, proc. SPIE* (Vol. 4153, pp. 151–158).

Wilson, S. R., & Forgan, B. W. (1995). *In situ* calibration technique for UV spectral radiometers. *Applied Optics*, *34*(24), 5475–5484. https://doi.org/10.1364/AO.34.005475

Xu, X., Wang, J., Zeng, J., Spurr, R. J. D., Liu, X., Dubovik, O., et al. (2015). Retrieval of aerosol microphysical properties from AERONET photopolarimetric measurements: 2. A new research algorithm and case demonstration. *Journal of Geophysical Research*, *120*, 7079–7098. https://doi.org/10.1002/2015JD023113

Yamamoto, G., & Tanaka, M. (1969). Determination of aerosol size distribution from spectral attenuation measurements. *Applied Optics*, *8*(2), 447–453. https://doi.org/10.1364/AO.8.000447

Yang, K., Carn, S. A., Ge, C., Wang, J., & Dickerson, R. R. (2014). Advancing measurements of tropospheric NO_2 from space: New algorithm and first global results from OMPS. *Geophysical Research Letters*, *41*, 4777–4786. https://doi.org/10.1002/2014GL060136

Zong, Y., Brown, S. W., Johnson, B. C., Lykke, K. R., & Ohno, Y. (2006). Simple spectral stray light correction method for array spectroradiometers. *Applied Optics*, *45*(6), 1111–1119. https://doi.org/10.1364/AO.45.001111

Zoogman, P., Liu, X., Suleiman, R. M., Pennington, W. F., Flittner, D. E., Al-Saadi, J. A., et al. (2017). Tropospheric emissions: Monitoring of pollution (TEMPO). *Journal of Quantitative Spectroscopy and Radiative*, *186*, 17–39. https://doi.org/10.1016/j.jqsrt.2016.05.008